15th International Symposium on Flow Visualization
June 25-28, 2012, Minsk, Belarus

VISUALIZATION OF SPATIO-TEMPORAL HEAT TRANSFER TO A TURBULENT FLOW

H. NAKAMURA[1,c], S. TAKAKI[2], S. YAMADA[1]

[1]Department of Mechanical Engineering, National Defense Academy, Yokosuka, 239-8686, Japan
[2] Graduate School of Science and Engineering, National Defense Academy, Yokosuka, 239-8686, Japan

[c]Corresponding author: Tel.: +81468413810; Fax: +81468445900; Email: nhajime@nda.ac.jp

KEYWORDS:
Main subjects: turbulent heat transfer, flow visualization
Fluid: low-speed air flow
Visualization method(s): infrared thermography, heated thin-foil
Other keywords: spatio-temporal measurement

ABSTRACT: The spatio-temporal distribution of quantitative heat transfer to a turbulent boundary layer was visualized by employing a technique using high-speed infrared thermograph and heated thin-foil. By solving the inverse problem, it was possible to restore the attenuation caused by thermal inertia and lateral conduction inside the wall. As a result, the spatio-temporal feature of the quantitative heat transfer caused by the wall turbulence was clearly revealed, which has hardly been clalified so far. In this paper, the procedure to estimate the heat transfer was presented, which included low-pass filter to reduce measurement noise, and inverse heat conduction analysis inside the test surface. The unique feature of the spatio-temporal heat transfer to the wall turbulence was also presented.

1. INTRODUCTION

Convective heat transfer is, by nature, generally nonuniform and unsteady, a fact reflected by flow turbulence. However, most experimental studies concerning the heat transfer between a solid wall and fluid have been performed in a time-averaged manner or using one-point measurements due to difficulties in the spatio-temporal measurements. Therefore, little is known experimentally so far on spatio-temporal feature of the heat transfer caused by flow turbulence.

Measurement techniques for time-space characteristics of the heat transfer have been developed using liquid crystal (Iritani et al., 1983) or using infrared thermography (Hetsroni and Rozenblit, 1994, Oyakawa et al., 2000, Nakamura and Igarashi, 2004), by employing a thin test surface having low heat capacity. However, the major problem of these measurements is attenuation of the temperature fluctuation due to the heat capacity of the test surface. Also, lateral conduction through the test surface attenuates the amplitude of the spatial temperature distribution. These attenuations are considerably large, especially for the heat transfer to air for which the heat transfer coefficient is low.

The recent improvement of infrared thermograph with respect to temporal, spatial and temperature resolutions enable us to investigate instantaneous temperature distribution and its fluctuating pattern on a solid surface caused by flow turbulence (Hetsroni et al., 2011, Golobic et al., 2012, Stafford et al., 2012). Although the thermo-images contain considerable attenuation in time and space due to thermal inertia and diffusion on the solid wall, it is possible to estimate quantitative heat transfer if the attenuation can be restored by solving inverse problem. In this paper, the procedure to estimate the quantitative heat transfer is presented, which includes low-pass filter to reduce measurement noise, and inverse heat conduction analysis inside the test surface. This procedure clearly revealed the spatio-temporal feature of the heat transfer to a turbulent flow.

NOMENCLATURE

l, l_{cut}	spatial wavelength, cutoff wavelength of low-pass filter $= 1/k_{cut}$
c	specific heat
f, f_{cut}	fluctuating frequency, cutoff frequency of low-pass filter
h	heat transfer coefficient

k, k_{cut} spatial wave number (m^{-1}), spatial cutoff wave number of low-pass filter
$\dot{q}$ heat flux
T temperature
T_0, T_w freestream and wall temperatures
ΔT_{IR} noise equivalent temperature difference of infrared thermograph $= \Delta T_{IR0}/\varepsilon_{IR}$
ΔT_{IR0} noise equivalent temperature difference of infrared thermograph for a blackbody
t time
u_0, u_τ freestream velocity, wall-friction velocity
x, y, z streamwise, vertical, and spanwise coordinates
α thermal diffusivity $= \lambda/(c\rho)$
δ thickness
ε_{IR} spectral emissivity for infrared thermograph
λ thermal conductivity
ν kinematic viscosity of fluid
ρ density

Subscript
a air
cd, cv conduction, convection
rd, rdi radiation to outside, radiation to inside

Other symbols
$(\bar{\ })$ mean value
$\Delta(\ )$, $(\ )_{rms}$ spatial or temporal amplitude, root-mean-square value

2. EXPERIMENTAL SETUP

The measurements were performed using a wind tunnel of 150 mm high × 400 mm wide, as shown in Fig. 1 (a). The freestream velocity ranged u_0 = 1 – 6 m/s, the turbulent intensity in this range was about 0.5 %. A flat plate of 890 mm long × 400 mm wide was set horizontally with a gap of 83 mm from the bottom of the wind tunnel. A test plate of 400 mm long × 360 mm wide was positioned behind the flat plate across a thermal insulator (acrylic resin prism of 10 mm

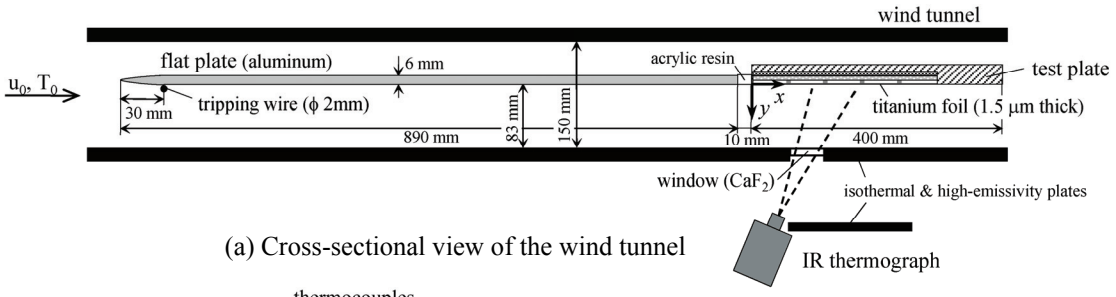

(a) Cross-sectional view of the wind tunnel

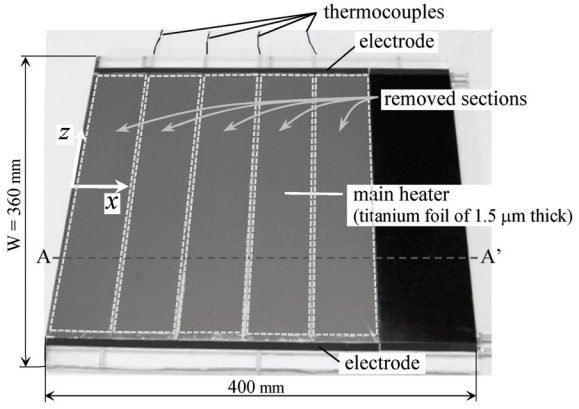

(b) Photograph of the test plate (lower face)

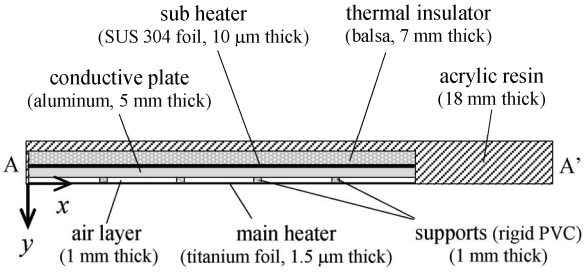

(c) Cross sectional view of the test plate

Fig. 1 Experimental Setup

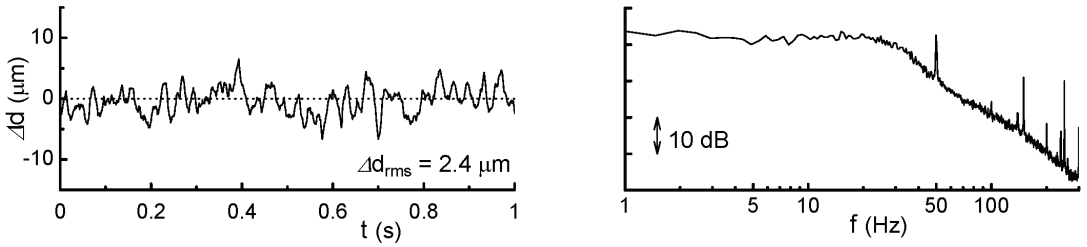

(a) Time trace of vertical displacement (b) Power spectrum of the vertical displacement

Fig. 2 Mechanical vibration of the titanium foil (u_0 = 6 m/s at flow reattaching region behind the backward-facing step)

streamwise length) so that there were no steps. At both spanwise ends of the test plate, there attached end plates having a sharp leading edge. A turbulent boundary layer was formed on the lower-side face of the flat plate by placing a tripping wire of 2 mm in diameter at 30 mm form the leading edge of the flat plate. The momentum thickness of the turbulent boundary layer on the unheated test plate at x = 207 mm was δ_θ = 3.02 – 2.84 mm, the wall-friction velocity and the wall-friction length were respectively $u_\tau = \sqrt{\nu\,|\partial\overline{u}/\partial y|}$ = 0.137 – 0.248 m/s and $l_\tau = \nu/u_\tau$ = 0.118 – 0.065 mm for the freestream velocity of u_0 = 3 – 6 m/s.

Figure 1 (b) and (c) show the photograph of the test plate and its cross-sectional view. The test plate was fabricated from acrylic resin having a hollow in the lower side. An aluminum plate of 5 mm thick was placed inside the test plate to impose a thermal boundary condition of a steady and uniform temperature. The lower face of the test plate was covered with five sheets of titanium foil of 1.5 μm thick and 61 mm wide, which were arranged in parallel between electrodes. Between the foils were fixed with supports of rigid PVC plates of 1 mm thick and 4 mm width. Between the foil and the aluminum plate, there exists an air clearance of 1.0 mm. The titanium foil was heated by applying a direct current under conditions of constant heat flux so that the temperature difference between the foil and the freestream to be about 30°C. In order to suppress the heat conduction loss to inside the plate, the aluminum plate was heated using a sub heater to keep the temperature difference between the titanium foil and the aluminum plate to minimize. Under these conditions, air enclosed by both the titanium foil and the aluminum plate does not convect because the Rayleigh number was below 10, which was much lower than the critical value of Ra_{cr}=1708 (Pellow & Southwell, 1940). Due to the existence of the air layer, the heat capacity of the heated surface was extremely low. This enabled us to observe the temperature fluctuation on the foil caused by turbulent heat transfer to outside the test plate.

To suppress a deformation of the heated thin-foil due to the thermal expansion of the air inside the plate, thin relief holes were connected from the ail-layer to the atmosphere. Also, the titanium foil was stretched by heating it since the thermal expansion coefficient of the titanium is smaller than that of the acrylic resin. This suppressed mechanical vibration of the foil against the fluctuation of the flow. Figure 2 (a) shows an example of the time trace of vertical displacement of the foil Δd due to the mechanical vibration, which was measured using a laser displacement meter (LK-G150, Keyence) at the flow reattaching region behind a backward-facing step at u_0 = 6 m/s (H = 30 mm, $x \approx$ 150 mm, $z \approx 0$: Nakamura, 2012). Although the pressure fluctuation for Fig. 2 (a) was much larger to that of the turbulent boundary layer examined here, the rms value of the displacement in the reattaching region was Δd_{rms} = 2.4 μm, which was one or two orders lower than the wall-friction length of the turbulent boundary layer. Figure 2 (b) shows the power spectrum corresponding to the fluctuation of Fig. 2 (a). This indicates that there seems to be no prominent peak due to the resonance effect at least up to 130 Hz (the peak at f = 50 Hz was the noise from power supply).

The infrared thermograph was positioned below the test plate and it measured the fluctuation of the temperature distribution on the lower-side face of the test plate through a CaF_2 window. In this study, a high-speed infrared thermograph (SC4000, FLIR) was employed. The frame rate was increased up to 1000 Hz by reducing the pixels to 160×168, while it was 420 Hz with a full resolution of 320×256 pixels. The value of NETD (noise equivalent temperature difference) in catalog was $\Delta T_{IR0} < 0.018$ K typically with an integration time (exposure time) of 0.961 ms.

The temperature on the titanium foil T_w was calculated using the following equation:

$$E_{IR} = \varepsilon_{IR} f(T_w) + (1 - \varepsilon_{IR}) f(T_a) \tag{1}$$

where E_{IR} is the spectral emissive power detected by the infrared thermograph, $f(T)$ is the calibration function of the infrared thermograph for a blackbody (Here, $f(T)$ was expressed by a cubic equation), ε_{IR} is spectral emissivity of the

titanium foil for the infrared thermograph, and T_a is the ambient wall temperature. [Since the CaF_2 window reflected and absorbed a part of the emissive power of about 5 %, the spectral emissivity ε_{IR} in Eq.(1) was the effective value.] The first and second terms in the right side of Eq.(1) represent the emissive power from the test surface and surroundings, respectively. In order to suppress the diffuse reflection and also to keep the second term to be uniform, the walls surrounding the heated surface were assembled by isothermal and high-conductivity plates (aluminum plates coated with black paint were used here). The thermograph was set with an inclination angle of 20° against the test surface in order to avoid the reflection of infrared radiation emitted from the thermograph itself.

The spectral emissivity of the foil, ε_{IR} (effective value), was estimated using the titanium foil, which was adhered closely to a heated copper plate. This plate was replaced with the test plate in Fig. 1 (a) and measured the emissive power from it using the infrared thermograph. The value of ε_{IR} can be calculated from Eq.(1) by substituting E_{IR} detected by the infrared thermograph, the copper plate temperature ($\approx T_w$) measured using such as calibrated thermocouples, and the ambient wall temperature T_a.

The accuracy of this measurement was verified to measure the distribution of mean heat transfer coefficient for a laminar boundary layer. The result was compared to a 2D heat conduction analysis assuming the velocity distribution to be a theoretical value. The agreement was very well (within 3 %), indicating that the present measurement is reliable to evaluate the heat transfer coefficient at least for a steady flow condition (Nakamura, 2007).

Also, a dynamic response of this measurement was investigated against a stepwise change of the heat input to the foil in conditions of a steady flow for a laminar boundary layer. The time response of the measured temperature agreed well to that of the numerical analysis of the heat conduction based on Eqs. (5) and (6). This indicates that the delay due to the heat capacity of the foil, $c\rho\delta(\partial T_w/\partial t)$ in Eq. (5), and the heat conduction loss to the air layer, $\dot{q}_{cd} = -\lambda_a (\partial T/\partial y)_{y=0-}$ in Eq. (5), can be evaluated with an acceptable accuracy (Nakamura, 2007).

3. EVALUATION OF MEASUREMENT NOISE

3.1 Measurement Noise in Thermo Images

Figures 3 (a) and 4 (a) show the time-spatial temperature distribution on the heated titanium foil for a laminar boundary layer (u_0 = 1 m/s) and for a turbulent boundary layer (u_0 = 4 m/s), respectively. Each of them, the left figure shows an instantaneous temperature distribution on the foil and the right shows a time trace of the spanwise distribution at x = 220 mm. For the laminar boundary layer for which the flow is steady and almost uniform, spatial region and temperature range are zoomed in to emphasize the measurement noise. The thermo image has two types of noise, one is temporal noise of a sensor resulting in the temperature fluctuation of a pixel, and the other is spatial noise due to unevenness of the sensor output resulting in the temperature scatter among pixels.

The temporal noise, which was defined as the rms value of the temperature fluctuation for the laminar case, was 0.05°C. This value was well below that estimated from the NETD, that is, $\Delta T_{IR} = \Delta T_{IR0}/\varepsilon_{IR} < 0.10$°C. In contrast, the spatial noise defined as the rms value of the temperature scatter in the instantaneous distribution for the laminar case was 0.11°C, which was higher than the temporal noise. In general, the spatial noise is higher than the temporal one for the focal plane array sensor, which is widely used nowadays for an infrared camera.

3.2 Noise Reduction

The finer-scale noise in the time-spatial distribution, as shown in Fig. 3 (a), affects significantly in calculating the time differential $\partial T_w/\partial t$ and space differentials $\partial^2 T_w/\partial x^2$ and $\partial^2 T_w/\partial z^2$ in Eq. (5). Thus, it is essential to reduce the finer-scale noise before calculating the inverse problem. To address this, a low-pass filter (sharp cutoff) was applied to the temporal (t) and the spatio (x and z) directions separately. The filter used here eliminates all frequencies (wavenumbers) above the cutoff frequency f_{cut} (cutoff wavenumber k_{cut}) while it passes unchanged below the f_{cut} (k_{cut}). Figure 3 (b) and Figure 4 (b) show the temperature distributions after applying the low-pass filter. Here, the cutoff frequency was set to f_{cut} = 200 Hz, which corresponds to the time interval of five flames of a series of the thermo images. The cutoff wavenumber of k_{cut} was set to 450 m^{-1} (cutoff wavelength of l_{cut} = 2.2 mm), which corresponds to the distance of six pixels of the thermo image. The values of f_{cut} and k_{cut} can be adjusted separately in order to reduce the noise effectively, while not attenuate the structure caused by flow turbulence. (This effect will be discussed later in Section 4.3.) As indicated in Fig. 3 (b), the finer structure in space and time becomes flatten, although the spatio-temporal structure due to the flow turbulence is almost unchanged after applying the filter, as indicated in Fig. 4 (b). Despite there still remains the spatial unevenness of a larger wavelength, as shown in Fig. 3 (b), the effect is not crucial in calculating the space

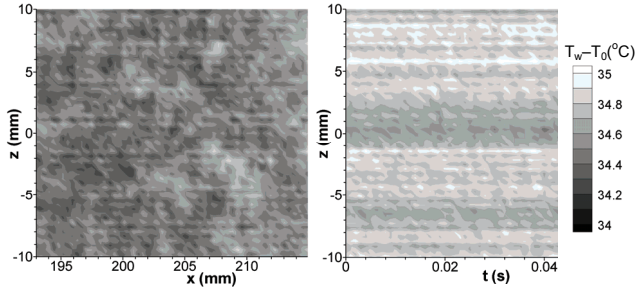

(a) Raw data
(left – *x*-*z* distribution; right – time trace of *z* distribution)

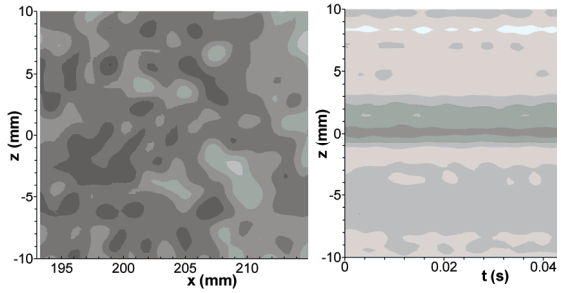

(b) After low-pass filter

Fig. 3 Temperature distribution of laminar boundary layer at u_0 = 1 m/s (indicates the measurement noise)

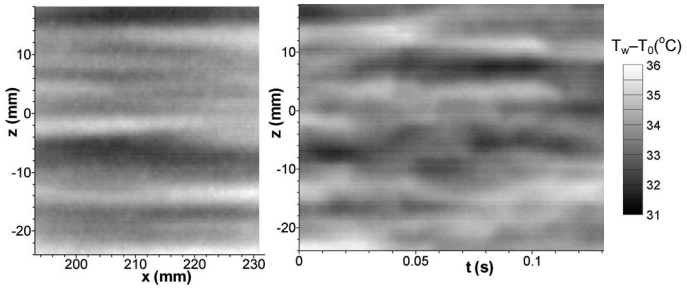

(a) Raw data
(left – *x*-*z* distribution; right – time trace of *z* distribution)

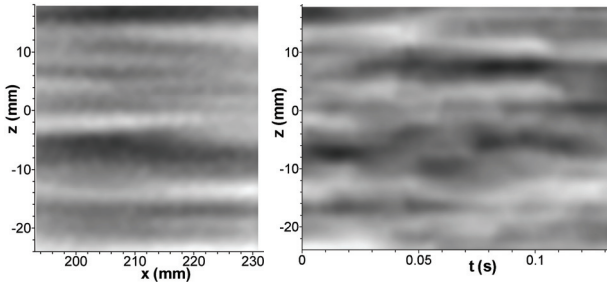

(b) After low-pass filter

Fig. 4 Temperature distribution of turbulent boundary layer at u_0 = 4 m/s caused by flow turbulence

differential in Eq.(5). However it is desirable to also reduce the larger-scale noise to improve the spatial S/N ratio, as described later in Fig. 5 (b). This may be possible by subtracting the time-averaged unevenness, which is the subject in future.

3.3 S/N Ratios

Figure 5 (a) shows the power spectrums of the temperature fluctuation for both signal (turbulent boundary layer) and noise (laminar boundary layer). Dotted lines denote the temperature without filter corresponding to Figs. 3 (a) and 4 (a), and solid lines denote the filtered temperature corresponding to Figs. 3 (b) and 4 (b). By applying the filter, the temporal noise was much reduced by about 10 dB, resulting in the S/N ratio to be greater than 1000 for f < 30 Hz, while it decreased to about 4 at the cutoff frequency of f_{cut} = 200 Hz. Figure 5 (b) shows the power spectrum of the spanwise temperature distribution. In this case, the S/N ratio was not as high as that for the temporal fluctuation since the spatial scatter was larger than the temporal fluctuation. Although the noise was reduced effectively by applying the filter for the smaller wavelength of $l < l_{cut}$ (= 2.2 mm), the noise for the larger wavelength was not reduced effectively. This is likely to be due to the considerable amount of the spatial noise whose wavelength is larger than l_{cut} = 2.2 mm, as indicated in Fig. 3 (b). Therefore, the S/N ratio was not high, which was about 100 for the wavelength of l > 10 mm, while it decreased to about 2 ~ 3 at the cutoff wavelength of l_{cut} = 2.2 mm.

Incidentally, the frequency response and spatial resolution of the measurement using infrared thermography and heated thin-foil was investigated analytically (Nakamura, 2009). It was reported that the upper limit of the detectable fluctuating frequency against noise, f_{max}, and the lower limit of the detectable spatial wavelength against noise, l_{min}, can be determined as a function of $\Delta h(\overline{T_w} - T_0) / \Delta T_{IR0}$ if thermophysical properties of the foil is specified. These values for the turbulent boundary layer (u_0 = 4 m/s, x = 220 mm) were f_{max} = 65 Hz and l_{min} = 1.0 mm (at Δh = 4.3 W/m^{2}K, $\overline{T_w} - T_0$ = 34°C, ΔT_{IR0} = 0.018°C, for a 1.5 μm thick titanium foil; Δh can be defined as h_{rms} if ΔT_{IR0} is defined as rms value). Although the cutoff frequency f_{cut} = 200 Hz was greater than f_{max}, the measurement was possible up to f_{cut} since the temporal noise was much reduced by applying the filter, as shown in Fig. 5 (a), in addition to the fact that the temporal noise was well below that estimated from ΔT_{IR0}. In contrast, the cutoff spatial wavelength l_{cut} = 2.2 mm was worse than l_{min}, which was mainly due to the large spatial noise. Also, the coarse pixel resolution was another reason, since the value l_{cut} needs at least the distance of six pixels to restore the spatial amplitude without a considerable attenuation, as described later in Fig. 6 (b).

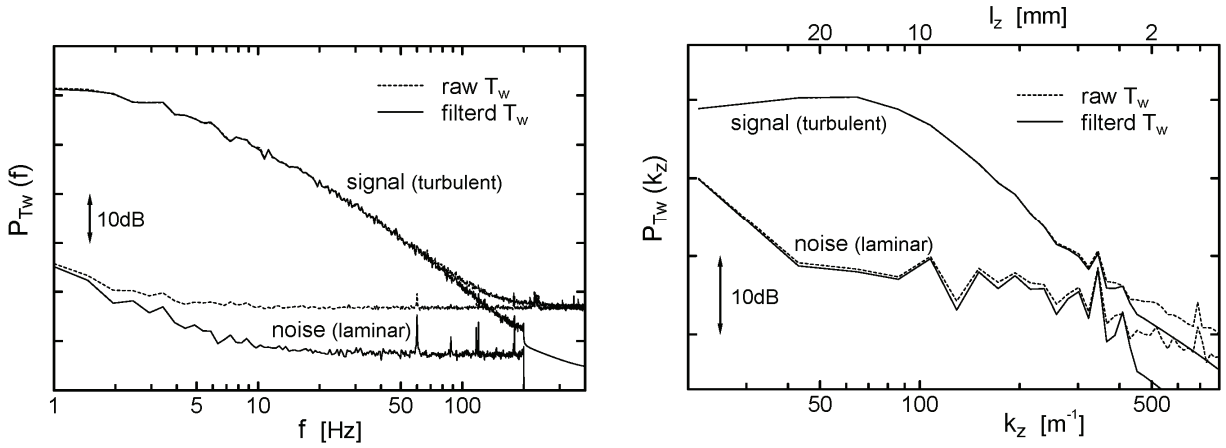

(a) Power spectrum of temperature fluctuation (b) Power spectrum of spanwise temperature distribution

Fig. 5 S/N ratios (signal – turbulent boundary layer at u_0 = 4 m/s; noise – laminar boundary layer at u_0 = 1 m/s)

4. RESTORATION OF SPATIO-TEMPORAL HEAT TRANSFER

4.1 Basic Equation and Finite Difference

Since the time-spatial distribution of the temperature on the foil attenuates in time and space due to the thermal inertia and diffusion, it is necessary to restore it to evaluate the quantitative heat transfer. This is possible by solving the inverse problem. The following describes the basic equation and the procedure to calculate the quantitative heat transfer.

Assuming that the temperature is uniform along its thickness, the heat balance on the titanium foil (thickness δ, specific heat c, density ρ, thermal conductivity λ) can be expressed as:

$$c\rho\delta\frac{\partial T_w}{\partial t}=\lambda\delta\left(\frac{\partial^2 T_w}{\partial x^2}+\frac{\partial^2 T_w}{\partial z^2}\right)+\dot{q}\ ,\ (y=0). \tag{2}$$

Here, T_w is local and instantaneous temperature of the foil. The heat flux, $\dot{q}$, is given by

$$\dot{q}=\dot{q}_{in}-\dot{q}_{cv}-\dot{q}_{cd}-\dot{q}_{rd}-\dot{q}_{rdi} \tag{3}$$

where $\dot{q}_{in}$ is the input heat-flux to the foil due to Joule heating, $\dot{q}_{cv}$ and $\dot{q}_{cd}$ are heat fluxes from the foil due to convection and conduction, respectively, $\dot{q}_{rd}$ and $\dot{q}_{rdi}$ are radiation heat flux to outside and inside the test plate, respectively. The convective heat flux is expressed using the heat transfer coefficient h as

$$\dot{q}_{cv}=h\,(T_w-T_0) \tag{4}$$

The local and instantaneous heat transfer coefficient was derived from Eqs. (2)-(4) as

$$h=\frac{\dot{q}_{in}-\dot{q}_{cd}-\dot{q}_{rd}-\dot{q}_{rdi}+\lambda\delta\left(\frac{\partial^2 T_w}{\partial x^2}+\frac{\partial^2 T_w}{\partial z^2}\right)-c\rho\delta\frac{\partial T_w}{\partial t}}{T_w-T_0} \tag{5}$$

This equation contains both terms of lateral conduction through the foil, λδ ($\partial^2 T_w/\partial x^2+\partial^2 T_w/\partial z^2$), and the delay due to the heat capacity of the foil, $c\rho\delta(\partial T_w/\partial t)$. Heat conduction to the air layer inside the wall, $\dot{q}_{cd}=-\lambda_a\,(\partial T/\partial y)_{y=0-}$ in Eq. (5), was calculated using the temperature distribution in the air layer (thickness δ_a), which can be determined by solving the heat conduction equation as follows (coordinate system is shown in Fig. 1).

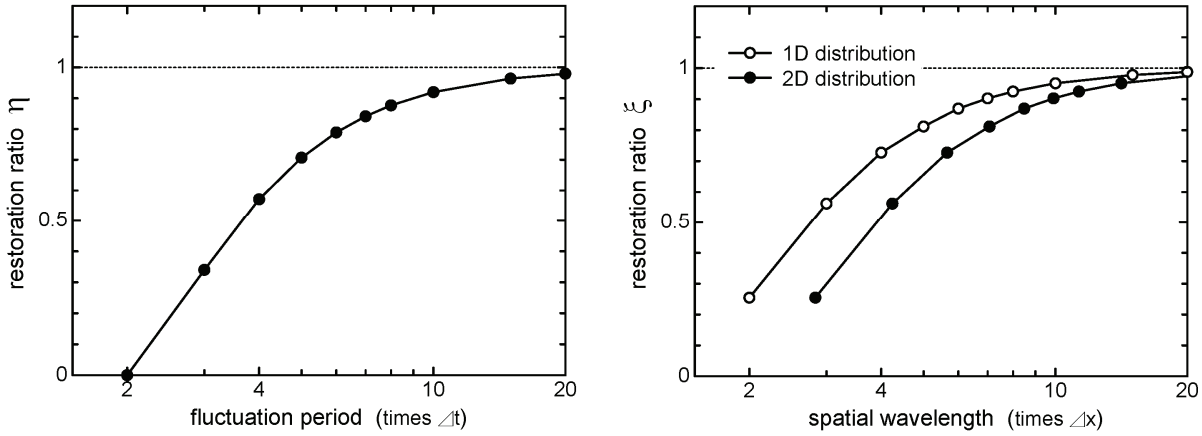

(a) In calculating $\Delta T_w/\Delta t$ (b) In calculating $\Delta^2 T_w/\Delta x^2$ and $\Delta^2 T_w/\Delta z^2$

Fig. 6 Restoration ratio of amplitude due to finite difference calculation

$$c_a \rho_a \frac{\partial T}{\partial t} = \lambda_a \left(\frac{\partial^2 T}{\partial x^2} + \frac{\partial^2 T}{\partial y^2} + \frac{\partial^2 T}{\partial z^2} \right), \quad (-\delta_a < y < 0) \tag{6}$$

Since the temperature of the aluminum plate inside the test plate is assumed to be steady and uniform, the boundary condition of Eq. (6) on the aluminum plate side ($y = -\delta_a$) can be assumed as a mean temperature of the aluminum plate measured using calibrated thermocouples.

The finite difference method was applied to calculate the heat transfer coefficient h from Eq. (5). The time derivative term $\Delta T_w/\Delta t$ was calculated using the central difference method, in which the time differential Δt was set to the frame interval of the thermo-images (Δt = 1.0 ms at the frame rate of 1000 Hz). The space derivative terms of $\Delta^2 T_w/\Delta x^2$ and $\Delta^2 T_w/\Delta z^2$ were calculated using the central difference of second order, where the space differentials Δx and Δz were set to the pixel pitch of the thermo-image ($\Delta x \approx \Delta z$ = 0.36 mm in the condition examined here). Eq. (6) was solved using ADI (alternative direction implicit) method (Peaceman and Rachford, 1955) with respect to x and z directions. The thickness of the air layer (δ_a = 1 mm) was divided into six regions (Δy = 0.13 mm) to satisfy $\Delta y < \sqrt{(\alpha_a/(\pi f_{cut})}$, which is the length to approximate the instantaneous temperature distribution to be linear up to f_{cut} = 200 Hz. (This relation was derived from the condition $\kappa\delta < 1$. See Fig. 2 in Ref. 11.)

4.2 Attenuation due to Finite Difference Calculation

The calculation of the derivative terms of $\Delta T_w/\Delta t$, $\Delta^2 T_w/\Delta x^2$, and $\Delta^2 T_w/\Delta z^2$ using the finite difference method accompanies temporal and spatial attenuation. Figure 6 (a) shows the restoration ratio of the fluctuating amplitude through the calculation of $\Delta T_w/\Delta t$. This was evaluated under a sinusoidal fluctuation of the heat transfer coefficient. The procedure was as follows: At first, the temperature fluctuation on the foil, T_w, was calculated by a 1D heat conduction analysis along y axis against a given fluctuation of the heat transfer coefficient at y = 0, by applying a sufficiently fine time step. Then, the heat transfer coefficient was calculated from Eqs. (5) and (6) using the calculated temperature fluctuation by applying the time step Δt, assuming that the temperature is uniform in x and z directions. The temporal restoration ratio η was defined as the amplitude of h calculated here against the original one. As shown in Fig. 6 (a), the temporal restoration ratio η is greater than 0.9 (attenuation is below 10 %) if the fluctuation period is larger than $10\Delta t$, while it decreases with decreasing the period.

Figure 6 (b) shows the restoration ratio of the spatial amplitude accompanied by the calculation of $\Delta^2 T_w/\Delta x^2$ and $\Delta^2 T_w/\Delta z^2$. This was evaluated under a 1D or 2D sinusoidal distribution of the heat transfer. The 2D distribution was expressed as $h = \bar{h} + \Delta h \sin(kx)\sin(kz)$. At first, the temperature distribution on the foil, T_w, was calculated by a steady heat conduction analysis against the given distribution of the heat transfer coefficient (1D or 2D) by applying a sufficiently fine mesh. Then, the heat transfer coefficient was calculated from Eqs. (5) and (6) using the calculated temperature distribution, by applying the space differences of Δx and Δz. As shown in Fig, 6 (b), the spatial restoration

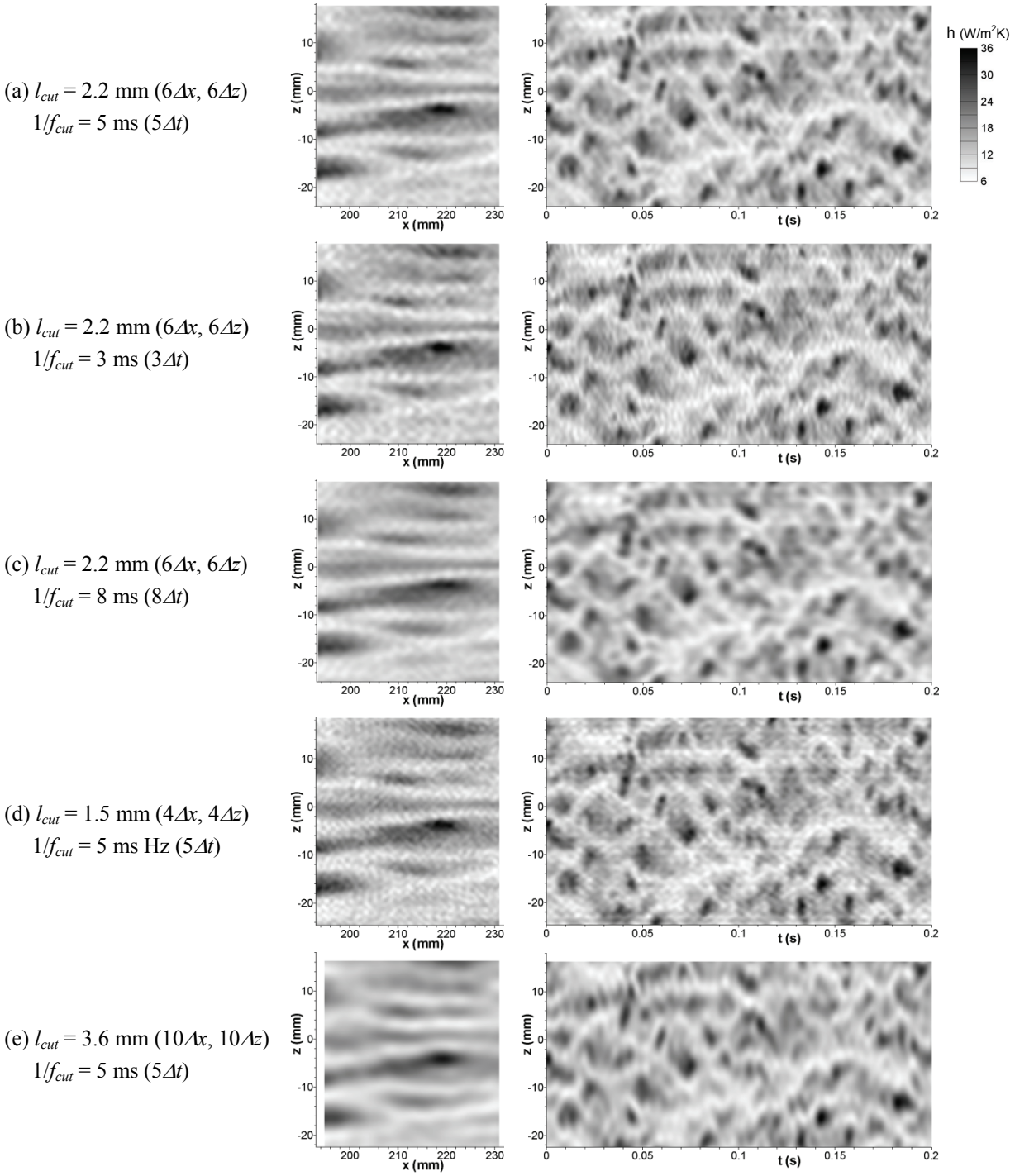

Fig. 7 Spatio-temporal distribution of heat transfer coefficient to the turbulent boundary layer corresponding to Fig. 4 (u_0 = 4 mm, Re_θ = 580: left – instantaneous distribution; right – time trace of z distribution at x = 220 mm)

ratio ξ for the 2D distribution is greater than 0.9 (attenuation is below 10 %) if the spatial wavelength is larger than 10Δx and 10Δz, while it decreases with decreasing the wavelength.

4.3 Spatio-Temporal Feature of the Quantitative Heat Transfer

The spatio-temporal distribution of the heat transfer coefficient corresponding to Fig. 4 (b), which was calculated using the procedure described in Sec. 4.1, is shown in Fig. 7 (a). The temporal distribution was restored up to $1/f_{cut} = 5\Delta t$ = 5 ms, at which the attenuation due to the finite difference calculation is 30 % as indicated in Fig. 6 (a). The temporal attenuation decreases below 10 % for the larger period of $1/f > 10\Delta t$ = 10 ms. The spatial distribution was restored up to

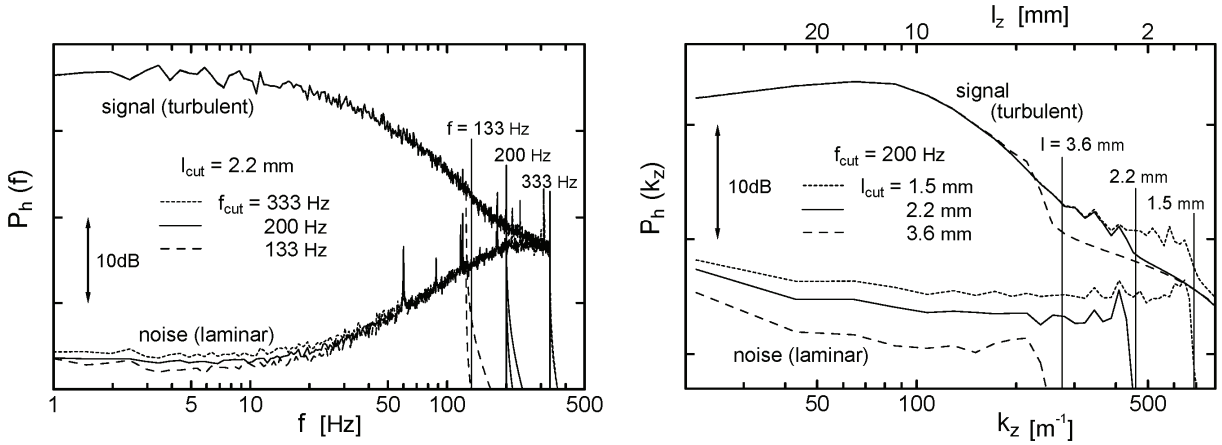

(a) Power spectrum of fluctuation (b) Power spectrum of spanwise distribution

Fig. 8 S/N ratios of the heat transfer coefficient
(signal – turbulent at u_0 = 4 m/s, $\overline{T_w} - T_0$ = 34°C; noise – laminar at u_0 = 1 m/s, $\overline{T_w} - T_0$ = 35°C)

$l_{cut} = 6\Delta x$ = 2.2 mm, at which the attenuation due to the finite difference calculation is 25 % as indicated in Fig. 6 (b). The spatial attenuation decreases below 10 % for the larger wavelength of $l > 10\Delta x$ = 3.6 mm. The cumulative power spectrum measured using a high-speed heat flux sensor indicated (not shown here), that the fluctuation of the heat flux within the frequency $f \leq 100$ Hz = $1/(10\Delta t)$ and $f \leq 200$ Hz = $1/(5\Delta t)$ accounts the 92 % and 99 % of the total fluctuating energy, respectively. Namely, it is reasonable to say that the spatial-temporal structure of the heat transfer caused by the flow turbulence was almost completely restored in Fig. 7 (a) without a considerable attenuation.

The spatio-temporal distribution of the heat transfer coefficient in Fig. 7 (a) has a feature reflected by the wall turbulence. The instantaneous distribution (left figure) is considered to be reflected by the well-known "streak" structure. The low heat transfer region (white region), which may be corresponded to the low-speed streaks, elongates along the streamwise direction with some meanderings. The mean spanwise wavelength of this structure estimated from auto-correlation was about 11 mm ≈ $120\nu/u_\tau$, which is roughly the same as the mean spanwise spacing between low-speed streaks reported by many researchers (around $100\nu/u_\tau$ typically). Also, it should be noticed that the high heat transfer region does not elongate monotonously but sometimes accompanies a spot of very high heat transfer. This is likely to be related to, so called the "bursting" phenomena, which produces most of the turbulence energy near the wall.

It is remarkable that the time trace of the heat transfer (right figure) reveals many maximum spots, which appears and disappears almost randomly in space and time, but has a characteristic period of an order of 10 ms. This feature is considered to be time-spatial characteristics of the "bursting". In fact, the mean period between the maximums at a single location, which was estimated from the pre-multiplied spectrum of the fluctuation, is 32 ms = $55\nu/u_\tau^2$. This is the same order as the mean period between the bursts reported in previously published literature, although the value has a considerable scatter among researchers.

Next, in order to investigate the effects of the cutoff wavelength l_{cut} and the cutoff frequency f_{cut} of the low-pass filter on the noise reduction, they were systematically varied to restore the spatio-temporal distribution. The results are shown in Fig. 7 (b) ~ (e), and that of the S/N ratio is shown in Fig. 8. If f_{cut} increases up to 333 Hz ($1/f_{cut} = 3\Delta t$), the temporal noise just below the f_{cut} becomes conspicuous, as shown in Fig. 7 (b). This is due to the remarkable increase in the noise with increasing the frequency, as shown in Fig. 8 (a), which suggests that the signal is not distinguishable anymore at around f = 333 Hz. This also affects the spatial noise at around l_{cut} = 2.2 mm, as shown Fig. 7 (b). Accordingly, the maximum cutoff frequency applicable is around f_{cut} = 200 Hz ($1/f_{cut} = 5\Delta t$) in this measurement conditions. In contrast, when f_{cut} decreases to 133 Hz ($1/f_{cut} = 8\Delta t$), the temporal noise is almost inconspicuous although some temporal blue occurs, as shown in Fig. 7 (c).

If the cutoff wavelength l_{cut} decreases to 1.5 mm (= $4\Delta x$), the spatial noise around l_{cut} becomes conspicuous, as shown in Fig. 7 (d). This is due to the increase in the noise with decreasing l_{cut}, as shown in Fig. 8 (b). Accordingly, the minimum cutoff wavelength applicable is around l_{cut} = 2.2 mm (= $6\Delta x$) in this measurement conditions. In contrast, when l_{cut} increases to 3.6 mm ($l_{cut} = 10\Delta x$), the spatial noise is almost inconspicuous although some spatial blue occurs, as shown in Fig. 7 (e).

As demonstrated here, the time-spatial structure of the heat transfer is shown to be consistent regardless of the parameters f_{cut} and l_{cut} of the low-pass filter, although the noise depends largely on the parameters, as shown in Fig. 7 (a) ~ (e). It follows from what has been said that the common feature in Fig. 7 (a) ~ (e) is the spatial-temporal distribution of the quantitative heat transfer caused by the wall turbulence, which has hardly been clarified experimentally so far.

5. CONCLUSIONS

A spatio-temporal distribution of the quantitative heat transfer to the turbulent boundary layer was visualized by employing a technique using high-speed infrared thermograph and heated thin-foil. By solving the inverse problem using the procedure described in this paper, it was possible to restore the local and instantaneous heat transfer coefficient up to $6\Delta x$ (= 2.2 mm) in space and $5\Delta t$ (= 5 ms, f = 200 Hz) in time with an attenuation below 30%, where Δx is pixel pitch of the thermo-image and Δt is the frame interval. As far as the structure larger than $10\Delta x$ (= 3.6 mm) and $10\Delta t$ (= 10 ms, f < 100 Hz), in which the most of the fluctuating energy included, the attenuation was less than 10%. Namely, the quantitative picture of the heat transfer caused by the wall turbulence was successfully revealed here without a considerable attenuation.

The heat transfer was dominated by the well-known “streak” structure near the wall. The low heat transfer region, which should be corresponded to the low-speed streaks, elongated along the streamwise direction with some meanderings. Also, the high heat transfer spot, which was likely to be reflected by the bursting phenomena, appeared almost randomly in space and time. The mean spanwise wavelength and the characteristic fluctuating period, which appeared in the heat transfer, reasonably agreed to the mean wavelength of the streaks and the mean period between the bursts reported in previously published literature.

References

1. Iritani Y., Kasagi N., and Hirata M. *Heat Transfer Mechanism and Associated Turbulent Structure in the Near-Wall Region of a Turbulent Boundary Layer*. 4th Symp. on Turbulent Shear Flows, 1983, pp. 17.31-17.36
2. Hetsroni G., Mosyal A., and Yarin P. T*hermal Streaks Regeneration in the Wake of a Disturbance in a Turbulent Boundary Layer*. Int. J. Heat and Mass Transf., 1997, **40**, p.4161
3. Oyakawa K., Miyagi T., Oshiro S., Senaha I., Yaga M., and Hiwada M. *Study on Time-Spatial Characteristics of Heat Transfer by Visualization of Infrared Images and Dye Flow*, Proc. 9th Int. Symp. on Flow Visualization, 2000, Pap. no. 233.
4. Nakamura H., and Igarashi T. *Unsteady heat transfer from a circular cylinder for Reynolds numbers from 3000 to 15000*. Int. J. Heat and Fluid Flow, 2004, **25**, p. 741
5. Golobic I., Petkovsek J. and Kenning D.B.R. *Bubble Growth and Horizontal Coalescence in Saturated Pool Boiling on a Titanium Foil, Investigated by High-Speed IR Thermography*, International Journal of Heat and Mass Transfer. 2012, **55**, p. 1385
6. Golobic I., Petkovsek J. and Kenning D.B.R. *Bubble Growth and Horizontal Coalescence in Saturated Pool Boiling on a Titanium Foil, Investigated by High-Speed IR Thermography*, International Journal of Heat and Mass Transfer. 2012, **55**, p. 1385
7. Stafford J. et al, *The Effect of Global Cross Flows on the Flow Field and Local Heat Transfer Performance of Miniature Centrifugal Fans*, International Journal of Heat and Mass Transfer. 2012, **55**, p. 1970
8. Pellow A. and Southwell R.V. *On Maintained Convective Motion in a Fluid Heated from Below*. Proceedings of the Royal Society A, 1940, **175**, p. 312
9. Nakamura H. Takaki S. and Yamada S. *Spatio-Temporal Characteristics of Heat Transfer for a Backward-Facing Step.* 7th Int. Symp. on Turbulence, Heat and Mass Transfer. 2012, Sicily, Italy, To be published
10. Nakamura H. *Measurements of Time-Space Distribution of Convective Heat Transfer to Air Using a Thin Conductive-Film.* 5th Int. Symp. on Turbulence and Shear Flow Phenomena. 2007, München, Germany, p. 773
11. Nakamura H. *Frequency-Response and Space-Resolution of a Thin Foil for Heat Transfer Measurements Using Infrared Thermograph*. Int. J. Heat and Mass Transfer, 2009, **52**, p. 5040
12. Peaceman D.W., and Rachford H.H. *The numerical solution of parabolic and elliptic differential equations*. J. Soc. Ind. Appl. Math., 1955, **3**, p.28